The Astrophysical Journal Letters, 883:L34 (7pp), 2019 October 1 https://doi.org/10.3847/2041-8213/ab4139

Discovery of a Red Supergiant Donor Star in SN2010da/NGC 300 ULX-1

M. Heida[1], R. M. Lau[2], B. Davies[3], M. Brightman[1], F. Fürst[4], B. W. Grefenstette[1], J. A. Kennea[5], F. Tramper[6], D. J. Walton[7], and F. A. Harrison[1]

[1] Cahill Center for Astronomy and Astrophysics, California Institute of Technology, 1200 East California Boulevard, Pasadena, CA 91125, USA; mheida@caltech.edu
[2] Institute of Space & Astronautical Science, Japan Aerospace Exploration Agency, 3-1-1 Yoshinodai, Chuo-ku, Sagamihara, Kanagawa 252-5210, Japan
[3] Astrophysics Research Institute, Liverpool John Moores University, Liverpool Science Park ic2, 146 Brownlow Hill, Liverpool L3 5RF, UK
[4] Quasar Ltd for ESA, European Space Astronomy Centre (ESA/ESAC), Operations Department, E-28692 Villanueva de la Cañada, Madrid, Spain
[5] Department of Astronomy and Astrophysics, Eberly College of Science, The Pennsylvania State University, 525 Davey Laboratory, University Park, PA 16802, USA
[6] IAASARS, National Observatory of Athens, Vas. Pavlou and I. Metaxa, Penteli 15236, Greece
[7] Institute of Astronomy, Madingley Road, Cambridge CB3 0HA, UK
Received 2019 August 1; revised 2019 August 27; accepted 2019 September 4; published 2019 September 25

Abstract

SN2010da/NGC 300 ULX-1 was first detected as a supernova impostor in 2010 May and was recently discovered to be a pulsating ultraluminous X-ray source. In this Letter, we present Very Large Telescope/X-shooter spectra of this source obtained in 2018 October, covering the wavelength range 350–2300 nm. The *J*- and *H*-bands clearly show the presence of a red supergiant (RSG) donor star that is best matched by a MARCS stellar atmosphere with $T_{\rm eff} = 3650$–3900 K and $\log(L_{\rm bol}/L_{\odot}) = 4.25 \pm 0.10$, which yields a stellar radius $R = 310 \pm 70 R_{\odot}$. To fit the full spectrum, two additional components are required: a blue excess that can be fitted either by a hot blackbody ($T \gtrsim 20{,}000$ K) or a power law (spectral index $\alpha \approx 4$) and is likely due to X-ray emission reprocessed in the outer accretion disk or the donor star; and a red excess that is well fitted by a blackbody with a temperature of ∼1100 K, and is likely due to warm dust in the vicinity of SN2010da. The presence of an RSG in this system implies an orbital period of at least 0.8–2.1 yr, assuming Roche-lobe overflow. Given the large donor-to-compact object mass ratio, orbital modulations of the radial velocity of the RSG are likely undetectable. However, the radial velocity amplitude of the neutron star is large enough (up to 40–60 km s^{-1}) to potentially be measured in the future, unless the system is viewed at a very unfavorable inclination.

Unified Astronomy Thesaurus concepts: High mass X-ray binary stars (733); Late-type supergiant stars (910); Neutron stars (1108)

1. Introduction

1.1. SN2010da

SN2010da in NGC 300 was initially discovered as a bright optical transient in 2010 May (Monard 2010). Subsequent multi-wavelength observations indicated that the transient was probably due to an outburst of a dust-enshrouded massive star rather than a supernova (Chornock & Berger 2010; Elias–Rosa et al. 2010; Prieto et al. 2010), which put it in the diverse category of supernova "impostors" or intermediate luminosity optical transients (ILOTs). These are distinct from typical core-collapse supernovae because the impostor progenitor survives the explosion, which exhibits typical peak absolute *V*-band magnitudes ranging from −11 to −14 (e.g., Van Dyk et al. 2000; Smith et al. 2009).

The progenitor of SN2010da was heavily obscured by dust; before 2010 May the system was detected in the mid-infrared (MIR) with the *Spitzer Space Telescope* (Lau et al. 2016), but pre-outburst optical observations yielded only upper limits (with the exception of a single detection in the *i*-band in 2008 September, at an AB magnitude of ∼24.2; Villar et al. 2016). Most of the dust seems to have been destroyed in the outburst, revealing a variable optical source with g', r', $i' \approx 20$–21; post-outburst observations also revealed re-brightening MIR emission (Lau et al. 2016; Villar et al. 2016).

The massive star in the system has been suggested to be a luminous blue variable (LBV; Binder et al. 2011, 2016), an sgB[e] star (Lau et al. 2016), or a yellow supergiant (Villar et al. 2016) based on its post-outburst photometry. Optical spectra of the source are dominated by emission lines indicative of ∼1000 km s^{-1} outflows and X-ray-ionized material, but no photospheric absorption lines from the star have been reported previously (Villar et al. 2016; Binder et al. 2018).

1.2. NGC 300 ULX-1

In the years following the 2010 outburst, a compact, persistent X-ray source was detected at the position of SN2010da with a 0.3–10 keV luminosity of 10^{36}–10^{37} erg s^{-1}. This led to the suggestion that the system could be a high-mass X-ray binary (HMXB), powered by accretion onto a black hole or neutron star (Binder et al. 2011, 2016). As this source was never detected in X-rays before the 2010 outburst, this may have been the first observed example of a massive binary evolving into an HMXB.

Then, in a deep *NuSTAR* +*XMM-Newton* observation taken in 2016, SN2010da was detected at a much higher X-ray luminosity of $\sim 5 \times 10^{39}$ erg s^{-1} (Carpano et al. 2018), above the threshold of 10^{39} erg s^{-1} for ultraluminous X-ray sources (ULXs; see Kaaret et al. 2017 for a recent review). Moreover, Carpano et al. (2018) discovered pulsations with a period of 31.6 s in its X-ray light curve, identifying SN2010da (now dubbed NGC 300 ULX-1; not to be confused with NGC 300 X-1, a Wolf–Rayet—black hole X-ray binary in the same galaxy) as a ULX pulsar. Only a handful of ULXs have been found to harbor neutron star accretors since the first ULX pulsar was discovered in 2014 (Bachetti et al. 2014), although similarities between the X-ray spectra of these pulsars and the general ULX population indicate that a majority of ULXs may

in fact contain neutron stars (Walton et al. 2018a). These systems offer an opportunity to study super-Eddington accretion flows and the role of the magnetic field. NGC 300 ULX-1 is the nearest of all currently known ULX pulsars, at a distance of 2.0 Mpc (Dalcanton et al. 2009), making it a valuable addition to this small sample.

Follow-up observations with *NuSTAR*, *Swift*, and *Chandra* in 2017 and early 2018 showed that both the pulsations and the super-Eddington luminosities were persistent during that time. Evidence for an ultra-fast outflow and possibly a cyclotron resonance feature was also found in deep *NuSTAR* and *XMM-Newton* observations (Kosec et al. 2018; Walton et al. 2018b). Regular monitoring showed that the source started to fade in the summer of 2018 and was no longer detected in short *Swift* observations as of 2019 May. NGC 300 ULX-1 was found to spin up very rapidly (at $\sim 10^{-7}$ s s^{-1}), and has one of the highest pulsed fractions seen in any ULX pulsar ($\sim$55% in the *XMM-Newton* data and increasing toward higher energies; Carpano et al. 2018). The pulse period evolution thus far shows no sign of orbital modulations, ruling out an orbital period that is shorter than a year (Ray et al. 2019; Vasilopoulos et al. 2018).

In this Letter, we present the near-ultraviolet (NUV) through near-infrared (NIR) spectrum of SN2010da/NGC 300 ULX-1 obtained with Very Large Telescope (VLT)/X-shooter when the source was fading in X-rays. We detect photospheric absorption lines in the NIR part of the spectrum, allowing us to reliably identify the donor star as a red supergiant (RSG). We also discuss the presence of two additional components in the broadband spectrum, as well as the properties of some of the emission lines that dominate the optical part of the spectrum.

2. Observations and Data Reduction

We obtained VLT/X-shooter (Vernet et al. 2011) spectra of the optical counterpart of NGC 300 ULX-1 (located at R.A. = 00:55:04.86, decl. = −37:41:43.7) observed in two identical observing blocks (OBs) as part of ESO programme 0102.D-0535(A), on 2018 October 10 and 12 (MJD 58402.1577 and 58404.2895). One of the OBs was also observed on October 9 but interrupted by a rapid response mode observation. We used the nod-on-slit mode with an ABBA nodding pattern and a nod throw of 3″. The slit widths are 0.″6 in the NIR arm, 0.″7 in the visible (VIS) arm and 0.″8 in the ultraviolet B (UVB) arm, yielding nominal spectral resolutions ($\lambda/\Delta\lambda$) of 8100, 11,400, and 6700, respectively. Each OB consists of 1 ABBA sequence with individual exposure times of 600 s in the NIR and UVB arms and 511 s in the VIS arm. This provides total exposure times of 4800 s in the NIR and UVB arms and 4088 s in the VIS arm. Seeing conditions were better than 0.″6 in the first OB and better than 0.″9 in the second, meaning that the actual spectral resolution for the first OB is set by the seeing rather than the slit width and is somewhat better than nominal, while for the second OB the spectral resolution is limited by the slit width.

We reduce the data with the standard ESO pipeline for X-shooter (v3.2.0) in Reflex (v2.9.1). We use nodding mode and standard settings for all steps except the extraction, where we set *extract_method* to localization and *localize_method* to manual, with *localize_slit_hheight* at 1.″5 for all arms. We also increase *crsiglim* to 10 for the VIS and UVB arms and 15 for the NIR arm.

We use Molecfit (Kausch et al. 2015; Smette et al. 2015) to correct the extracted VIS and NIR arm spectra for telluric absorption. In all bands, the flux is a few percent (4.5%, 3.5%, and 9% in the NIR, VIS, and UVB arms, respectively) higher in the first epoch, most likely due to slit losses in the second epoch with slightly worse seeing. We combine the two epochs by simple weighted averaging after applying the barycentric velocity correction and scaling the fluxes of the second epoch up to match those of the first epoch. The full spectrum is shown in Figure 1.

3. Analysis and Results

3.1. The Donor Star

The NIR part of the spectrum, redward of $\sim$700 nm, is dominated by absorption features that are typical of cool stars. Most prominent are the CO bandheads in the *H*- and *K*-bands and many molecular and atomic lines in the *J*- and *H*-bands. Meanwhile, in the optical one of the characteristic TiO absorption bands is visible (see Figure 2). These spectral features all point to the companion being a luminous, cool star (e.g., Meyer et al. 1998).

To obtain a temperature for the companion, we concentrate on the *H*-band region of the spectrum. The TiO features in the optical are well-known to be poorly reproduced by 1D model atmospheres (Davies et al. 2013), while the *K*-band emission from NGC 300 ULX-1 is contaminated by dust emission, which makes the stellar continuum difficult to place. The features that we concentrate on in the *H*-band are the CO bandheads, which are known to be sensitive to effective temperature (e.g., Davies et al. 2009, see Figure 3).

The model grid that we employ consists of synthetic spectra computed from MARCS model atmospheres (Gustafsson et al. 2008) using TURBOSPECTRUM (Plez 2012). We investigate effective temperatures $T_{\rm eff}$ in the range 3400–4400 K, and gravities $\log g$ between 0.0 and +1.0. For metallicity [*Z*], we compare the location of ULX-1 to the radial metallicity gradient as measured by Gazak et al. (2015), which indicates a value of $[Z] \simeq -0.1$. Therefore, we explore metallicities between $[Z] = 0.0$ to −0.25. Finally, we search microturbulent velocities ξ between 2 and 5 km s^{-1}, noting that the typical value for RSGs seems to be around 4 km s^{-1} (Davies et al. 2015).

Our methodology is to fix $\log g$, ξ and [*Z*], and find the best-fit $T_{\rm eff}$ using χ^2-minimization comparing the flux levels around the CO bandheads. We then repeat for all combinations of $\log g$, ξ, and [*Z*] within our permitted parameter space to find the full possible range of $T_{\rm eff}$ values. Irrespective of the combinations of $\log g$, ξ and [*Z*], we consistently find temperatures within the range $3650 < T_{\rm eff}/K < 3900$.

To find the luminosity $L_{\rm bol}$ of the companion, we assume that the RSG dominates the flux in the *H*-band (this is justified by our broadband fit, see Figure 1). We then use the *H*–*K* colors of the best-fitting models to estimate the *K*-band flux of the star. Because the bolometric correction (BC) at *K* is roughly the same for all RSGs ($\mathrm{BC}_K \simeq 3$, e.g., Davies et al. 2013, 2018), this then allows us to estimate a luminosity for the companion of $\log(L_{\rm bol}/L_\odot) = 4.25 \pm 0.10$. Converting the effective

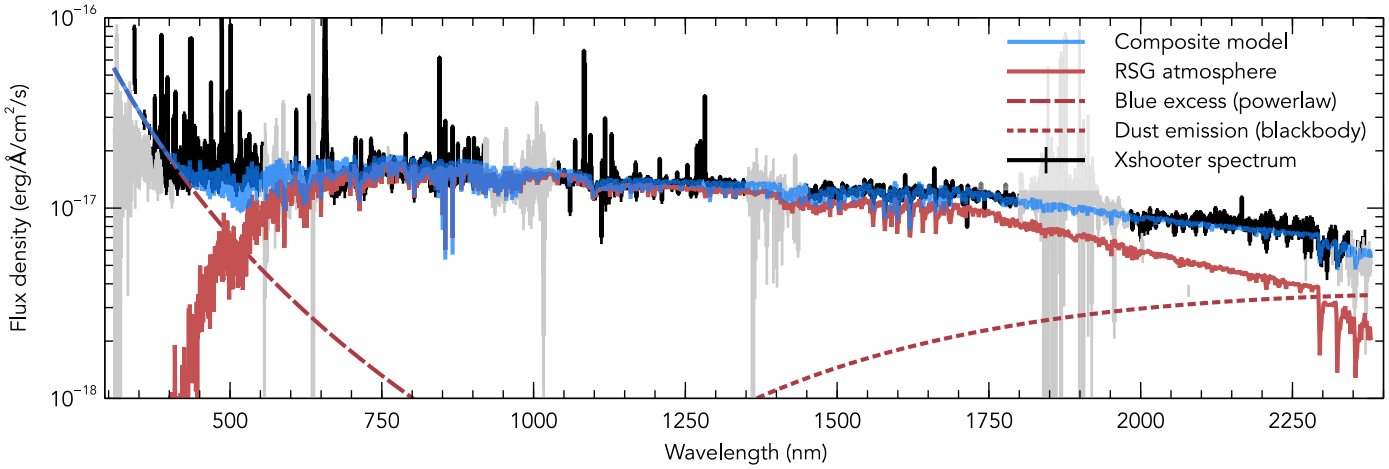

Figure 1. Full X-shooter spectrum (black, with errorbars) with areas heavily affected by telluric emission lines shown in gray. Overplotted are the best-matching MARCS model atmosphere (solid red line), a 1100 K blackbody to account for excess red emission (red dotted line) and a power law with $\alpha \approx 4$ to account for excess blue emission (red dashed line, although the shape of this component is not well constrained and can also be fit with a blackbody with $T \gtrsim 20{,}000$), as well as the sum of those three models (blue line). The large majority of positive outliers shown in black are emission lines, not noise.

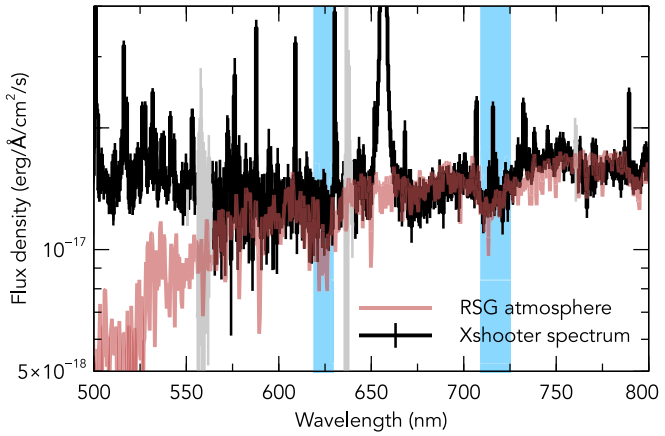

Figure 2. X-shooter data (black, with errorbars) in the 500–800 nm region containing TiO absorption features (indicated by the blue shaded regions; only the feature at 720 nm is visible in the data). Data points with low signal-to-noise ratio (S/N) are plotted in gray. The best-matching MARCS model atmosphere is overplotted in red. Blueward of 650 nm the data start to deviate from the model atmosphere—an extra model component is necessary to fit this excess blue emission.

temperature and luminosity to an equivalent radius R, we find $R/R_{\odot} = 310 \pm 70$.

We determine the radial velocity of the RSG through a cross-correlation of the X-shooter spectrum and the best-matching model atmosphere, using small regions around the strongest absorption lines in the 1150–1350 nm range. We find a radial velocity of $106 \pm 8\,\mathrm{km\,s^{-1}}$ (not corrected for the bulk motion of NGC 300 of $\sim$144 $\mathrm{km\,s^{-1}}$; Westmeier et al. 2011).

Two additional components are necessary to fit the full X-shooter spectrum (see Figure 1). Blueward of 700 nm the continuum emission is dominated by an additional blue component, and there is also excess emission redward of 1700 nm. The blue component can be represented by either a hot blackbody ($T \gtrsim 20{,}000$ K) or a power law with spectral index $\alpha \approx 4$; the signal-to-noise ratio (S/N) of the blue end of the X-shooter spectrum is too low to discriminate between these two options. The additional red component is well fitted by a blackbody of $\sim$1100 K.

3.2. Emission Lines

The optical spectrum of NGC 300 ULX-1 is dominated by many emission lines that are not connected to the donor star. A full analysis of these lines will be presented in a separate paper; we focus here on the Hα and He II λ4686 lines that were also analyzed by Binder et al. (2018). All velocities mentioned below are relative to the rest wavelength in air of the respective lines. We did not correct for the bulk motion of NGC 300.

3.2.1. Hα Line

The Hα line in the spectrum of NGC 300 ULX-1 is best fit by three components: a narrow Gaussian with an FWHM of $28.1 \pm 0.5\,\mathrm{km\,s^{-1}}$, centered at $109.54 \pm 0.17\,\mathrm{km\,s^{-1}}$ (656.5158 ± 0.0003 nm); a broad Lorentzian with an FWHM of $376 \pm 3\,\mathrm{km\,s^{-1}}$, centered at $121.4 \pm 0.6\,\mathrm{km\,s^{-1}}$ (656.5396 ± 0.0014 nm); and a second intermediate-width redshifted Gaussian with an FWHM of $102.3 \pm 1.5\,\mathrm{km\,s^{-1}}$, centered at $155.9 \pm 0.7\,\mathrm{km\,s^{-1}}$ (656.6160 ± 0.0015 nm; see Figure 4). The total observed flux in the line is $(8.76 \pm 0.08) \times 10^{-16}\,\mathrm{erg\,cm^{-2}\,s^{-1}}$. The equivalent width of the Hα line is -69.47 ± 0.03 Å. The spectral resolution in the VIS arm corresponds to a velocity resolution of $26\,\mathrm{km\,s^{-1}}$. The intrinsic FWHM is $10.6 \pm 0.5\,\mathrm{km\,s^{-1}}$ for the narrow Gaussian component, $375 \pm 3\,\mathrm{km\,s^{-1}}$ for the broad Lorentzian, and $99.0 \pm 1.5\,\mathrm{km\,s^{-1}}$ for the intermediate-width Gaussian. We fit the same three-component model to the individual epochs to check if shifts in the line velocities are a cause of broadening, but we do not find any variability in the central wavelengths and FWHM of the three line components.

3.2.2. He II Line

The He II line at 4686 Å is best fit by a Lorentzian with an FWHM of $116 \pm 4\,\mathrm{km\,s^{-1}}$, centered at $93.0 \pm 1.3\,\mathrm{km\,s^{-1}}$ (468.720 ± 0.002 nm; see Figure 5). The observed flux in the line is $(2.40 \pm 0.08) \times 10^{-17}\,\mathrm{erg\,cm^{-2}\,s^{-1}}$. The equivalent width of the line is -1.63 ± 0.06 Å. The spectral resolution in the VIS arm corresponds to a velocity resolution of $45\,\mathrm{km\,s^{-1}}$. The intrinsic FWHM of the He II line is $107 \pm 4\,\mathrm{km\,s^{-1}}$.

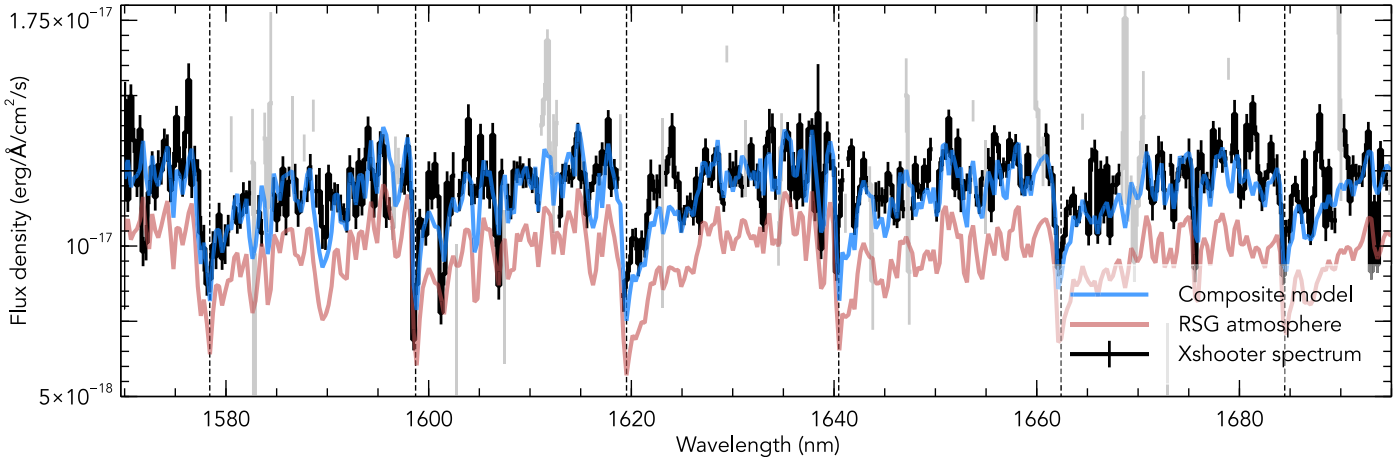

Figure 3. X-shooter data (black, with errorbars) in the 1575–1700 nm region containing several strong absorption features, most prominent of which are the CO bandheads (indicated with black dashed lines). Data points that are affected by strong telluric emission lines are plotted in gray. Overplotted are the best-matching MARCS model atmosphere (red) and the composite model including an 1100 K blackbody to account for excess emission (blue).

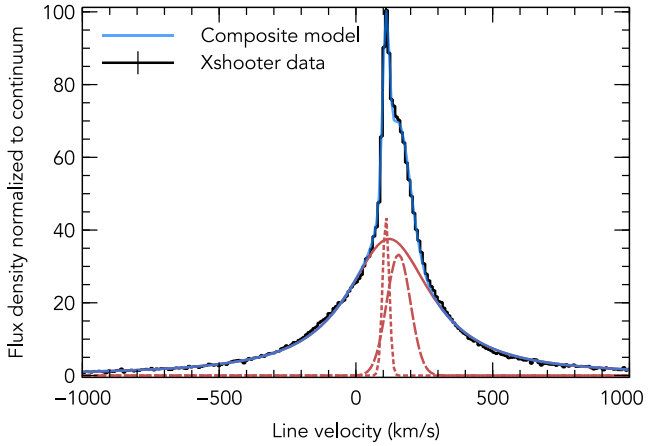

Figure 4. Hα line normalized to the continuum flux and shifted to a continuum of zero (black line with errorbars). The zero-point of the line velocity is at 656.276 nm. The three model components are plotted in red (narrow Gaussian, dotted line; redshifted, broader Gaussian, dashed line; broad Lorentzian, solid line) and the total model is plotted in blue.

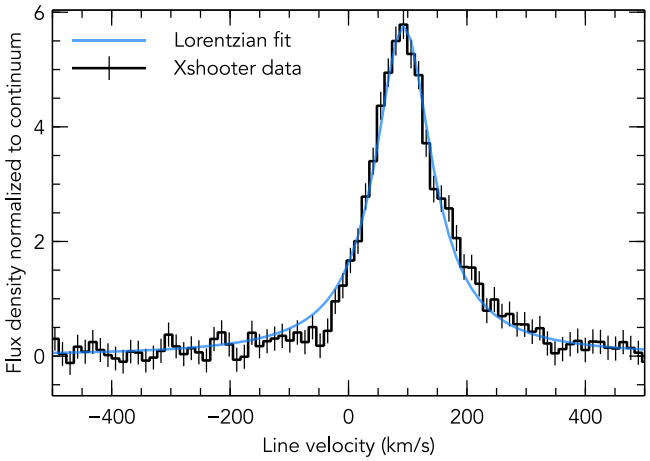

Figure 5. He II line normalized to the continuum flux and shifted to a continuum of zero (black line with errorbars). The zero-point of the line velocity is at 468.575 nm. The Lorentzian fit to the line is plotted in blue.

4. Discussion and Conclusions

4.1. The Nature of the Donor Star

The shape of the continuum in the 750–1700 nm region of our X-shooter spectrum, combined with the properties of the absorption bands due to TiO and CO and the many absorption lines due to neutral metals, allow us to determine the properties of the donor star in NGC 300 ULX-1 for the first time. We find an effective temperature of 3650–3900 K and a bolometric luminosity $\log(L/L_{\odot}) = 4.25 \pm 0.1$, which implies an RSG with a radius of $310 \pm 70\ R_{\odot}$. The radial velocity of the star is $106 \pm 8\ \mathrm{km\,s^{-1}}$, consistent with the RSG being located in NGC 300 (which has a radial velocity of $144\ \mathrm{km\,s^{-1}}$ and a maximum rotational velocity of $99\ \mathrm{km\,s^{-1}}$ Westmeier et al. 2011).

The connection between this RSG and the ULX is very secure. The position of the system that underwent the outburst in 2010 is accurately known (Monard 2010). Non-detections of the progenitor in optical bands and consistent detections of the source in the optical post-outburst, in combination with its MIR behavior, indicate a dust-enshrouded progenitor system that became visible at optical wavelengths after most of the dust was destroyed in the 2010 outburst (Lau et al. 2016; Villar et al. 2016). *Hubble Space Telescope* (*HST*) observations show the post-outburst optical source to be fairly isolated, and it is by far the brightest source in a 0.″5 radius—there is no other source nearby that could have contaminated our X-shooter spectra (see Figure 6). In addition, Binder et al. (2016) showed that the counterpart of SN2010da is the only optical source within the localization error of the ULX. The presence of emission lines, in particular the He II λ4686 line that is excited by X-ray photons, is additional evidence that the RSG and X-ray source belong to the same system.

The identification of the donor star as an RSG has important implications both for the current state of the system and for the interpretation of the 2010 supernova impostor event. Previous donor star identifications, all based on photometric observations in different bands, have included an LBV (Binder et al. 2016), an sgB[e] star (Lau et al. 2016), and a yellow supergiant (Villar et al. 2016, who did point out that the spectral energy distribution was consistent with an RSG as well but preferred a

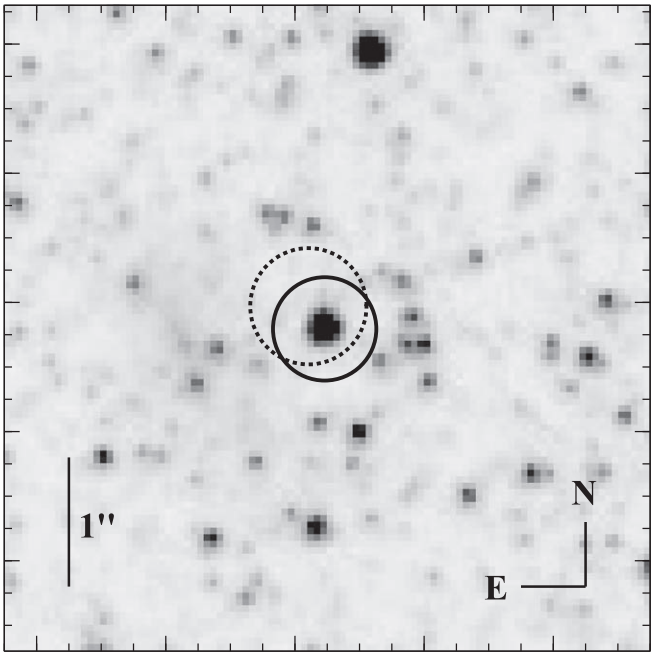

Figure 6. *HST* F814W image taken post-outburst in 2014 July with the location of the X-ray source from *Chandra* (0.″47 radius, dotted error circle; Binder et al. 2016). The solid circle centered on the optical source has a diameter of 0.″8, the size of the widest X-shooter slit that we used, showing that there are no other sources contributing significantly to the optical/NIR emission.

yellow supergiant based on the radius of the blackbody in the 2010 outburst). The presence of an RSG necessitates a fairly wide binary system, and the large donor-to-compact object mass ratio —given that typical RSG masses are $\geqslant 8\ M_{\odot}$—means that stable Roche-lobe overflow may not be possible (van den Heuvel et al. 2017, but see also Quast et al. 2019). The slow wind speeds in RSGs (typically 20–30 km s^{-1}, Richards & Yates 1998; van Loon et al. 2001) make NGC 300 ULX-1 a good candidate for focused wind accretion in a near-Roche-lobe overflow system, as suggested by, for example, El Mellah et al. (2019).

4.2. Orbital Parameters

The orbital period of NGC 300 ULX-1 is unknown. Contrary to other ULX pulsars, whose orbital periods have been determined or constrained from Doppler shifts of the pulse period (Bachetti et al. 2014; Israel et al. 2017; Fürst et al. 2018; Rodríguez Castillo et al. 2019; Sathyaprakash et al. 2019), the pulse period evolution of NGC 300 ULX-1 shows no sign of orbital modulations (Ray et al. 2019; Vasilopoulos et al. 2018). This is due in part to the very high absolute spin-up rate, which makes it difficult to detect small modulations to the spin period due to orbital motions.

The effective temperature and luminosity of the donor star are consistent with MESA evolution tracks of 8–10 $M_{\odot}$ single stars (Choi et al. 2016). We use this as our best estimate for the mass of the donor star, with the caveat that this star evolved in an interacting binary system and, moreover, experienced a large outburst just a few years ago. A detailed investigation of its evolutionary history is necessary to truly determine its mass, but is beyond the scope of this Letter.

Assuming an RSG with a mass of 8–10 $M_{\odot}$ and a radius of $310 \pm 70\ R_{\odot}$, and a neutron star of 1.4–2.0 $M_{\odot}$, we can calculate the orbital period at which the RSG would fill its Roche lobe (Eggleton 1983). For these parameters, the Roche-lobe filling orbital period would be 0.8–2.1 yr, which is consistent with the constraints from X-ray timing measurements of the pulse period (orbital period $\geqslant$1 yr, Ray et al. 2019; Vasilopoulos et al. 2018) and with the possible MIR period of ~400 days suggested by Lau et al. (2016). The orbital velocity of the RSG would be 8–10 km s^{-1}, and the orbital velocity of the neutron star 40–62 km s^{-1}. If the donor star is more massive, the orbital period would be even longer and the orbital velocities lower. The radial velocities of the two components are given by $v_{\rm orb}\sin(i)$; unless we are viewing the system at very low inclination, it is extremely unlikely that we will be able to detect radial velocity shifts for the RSG—particularly because convective motions in RSG atmospheres can produce radial velocity shifts of similar magnitude (Ohnaka et al. 2017), which would make any radial velocity curve of the RSG unreliable unless the orbital period is confirmed independently. The radial velocity of the neutron star is likely high enough to be measured unless the system is seen at a very unfavorable inclination, either through pulsar timing if the absolute spin-up decreases sufficiently such that the orbital modulations become detectable, or through radial velocity shifts of emission lines that are formed in the accretion disk and co-moving with the neutron star. However, this measurement will be extremely challenging due to the long orbital period of the system, requiring many years of monitoring; the emission line radial velocity method specifically has been attempted before for other ULXs but radial velocity variations were found to be essentially random (Roberts et al. 2011).

These numbers are in fact lower (upper) limits for the period (orbital velocities), as we do not know whether or not mass accretion occurs through Roche-lobe overflow in NGC 300 ULX-1. If the neutron star is instead accreting material from the wind of the RSG (as suggested by, e.g., El Mellah et al. 2019) the orbital period may be longer and the radial velocities lower.

4.3. Additional Broadband Components

The broadband spectrum can only be fit by adding two extra components, a blue component that dominates the emission blueward of ~700 nm and a red component that dominates the *K*-band emission. The excess red emission is also observed in *Spitzer* observations (Lau et al. 2016, 2019) and is consistent with being due to warm dust with a temperature of ~1100 K. The presence of excess blue emission is consistent with predictions from theory (e.g., Copperwheat et al. 2005; Ambrosi & Zampieri 2018), and is likely due to an irradiated accretion disk and/or irradiation of the donor star by the bright X-ray source. The strong variability of NGC 300 ULX-1 in X-rays indicates that this component, if it is indeed due to reprocessed X-ray emission, may be variable as well. Our X-shooter spectra were taken during a decrease of the X-ray flux of NGC 300 ULX-1 (see, e.g., the *Swift* light curve in Vasilopoulos et al. 2019); future observations taken at different X-ray flux levels are necessary to test this hypothesis.

4.4. Emission Line Structure

The structure of the Balmer emission lines is best described with three components: a narrow Gaussian component, a broad Lorentzian that is redshifted by ~15 km s^{-1} with respect to the narrow Gaussian, and an intermediate-width second Gaussian redshifted ~45 km s^{-1}. This structure, with a narrow, broad, and redshifted intermediate component, strongly resembles the

line structure observed two weeks after the 2010 outburst by Villar et al. (2016), although both the intermediate Gaussian and broad Lorentzian components have become considerably narrower; their FWHM decreased from $\sim$500 km s^{-1} to $\sim$100 km s^{-1} and from $\sim$1000 km s^{-1} to $\sim$375 km s^{-1}, respectively. The intermediate Gaussian component has also become less redshifted with respect to the narrow component, from $\sim$140 km s^{-1} in 2010 to $\sim$45 km s^{-1} now. Villar et al. (2016) modeled their late-time spectra as single Gaussians with an FWHM ranging from 300 to 600 km s^{-1} and an extended red wing, but these spectra were taken at lower resolution that likely precluded the detection of, for example, the additional narrow component.

Villar et al. (2016) suggested that the narrow component seen in their early spectra was due to a pre-existing wind from an earlier RSG phase, while the intermediate-width emission was powered by wind mass loss from the (blue or yellow supergiant) star post-outburst. Our identification of the post-outburst star as an RSG supports the claim that the narrow component of the Balmer emission lines is due to an RSG-driven wind; its FWHM of 10 km s^{-1} matches typical RSG wind speeds (Richards & Yates 1998; van Loon et al. 2001). This interpretation is also supported by the fact that the radial velocity of this component matches the radial velocity of the star itself. Alternatively, the narrow component could be due to a surrounding photoionized nebula as seen in other ULXs (e.g., Pakull & Mirioni 2002; Moon et al. 2011).

The intermediate-width emission is too broad to be due to a persistent stellar wind driven by the RSG, but its width is consistent with shock-ionized ULX bubbles (Pakull et al. 2010). An ultra-fast outflow (at 0.22c) was detected in this system in X-rays by Kosec et al. (2018), showing that strong winds are launched from the disk. Either the intermediate or broad Hα component may be due to a slower and cooler disk wind (similar broad hydrogen and sometimes helium emission lines have been detected in other ULXs and interpreted as evidence for a disk wind, Fabrika et al. 2015). One of these components may also be associated with material expelled by the star in the 2010 outburst.

4.5. He II Line Luminosity

The luminosity in the He II λ 4686 line can be used to infer the ionizing flux in the 54–200 eV range and, in combination with the measured X-ray flux in that range, to determine the beaming factor of the soft X-rays, as the He II emission is isotropic (Pakull & Angebault 1986). Binder et al. (2018) performed this calculation for NGC 300 ULX-1 using their Gemini spectra and simultaneous *Swift* observations obtained in 2017 June and July, when the source was in the ULX regime; they found that the number of He-ionizing photons calculated from the He II luminosity and from the X-ray luminosity (calculated from the X-ray flux assuming isotropic emission) were roughly equal, within a factor of two. This indicates that in the super-Eddington state, the soft X-rays (below 0.2 keV) were not strongly beamed, in contrast with the higher energy X-rays that must be more strongly beamed given the high pulsed fraction in NGC 300 ULX-1 (up to $\sim$76% above 2 keV, Carpano et al. 2018). It also shows that the He II-emitting gas surrounds the ULX with a covering factor close to one.

NGC 300 ULX-1 was monitored regularly in the X-rays with *Swift* in 2017 and 2018. Vasilopoulos et al. (2019) showed that the X-ray luminosity was stable at a level of $\sim 5 \times 10^{39}$ erg s^{-1} until 2018 February, when it started to drop until it settled down at around the Eddington luminosity of a neutron star, a factor $\sim$25 lower than its peak luminosity, in 2018 September (their Figure 1). It was still at this lower X-ray flux at the time our X-shooter spectra were taken in October. *NICER* and *Swift* observations of the pulse period obtained in 2018 August and November, when the source rebrightened in X-rays for a short time, show that the spin-up rate of the pulsar remained constant throughout 2018 (at $\dot{\nu} \approx 4 \times 10^{-10}$ s^{-2}) and did not vary with the X-ray flux, as would be expected if the flux decrease was due to a decrease in the mass accretion rate (Ray et al. 2019; Vasilopoulos et al. 2019). In addition, the ratio of 0.3–1.5 keV to 1.5–10.0 keV photons, as seen by *Swift*, did not change when the X-ray flux dropped, as would be expected if the source had undergone a state change or if the obscuring column density had increased. Vasilopoulos et al. (2019) suggested that the observed lower X-ray flux was due to increased obscuration by an optically thick outflow from the radiation-dominated inner accretion disk that moved into our line of sight due to Lense-Thirring precession.

The flux that we measure in the He II line in our October 2018 spectrum corresponds to a luminosity of $1.19 \pm 0.04 \times 10^{34}$ erg s^{-1}, after correcting the line flux for foreground Galactic extinction ($E(B-V) = 0.011$; Schlafly & Finkbeiner 2011) and assuming a distance of 2.0 Mpc to NGC 300. This is a factor of $\sim$70 lower than the luminosity reported by Binder et al. (2018), and the ionizing photon flux in the 54–200 eV range inferred from this line luminosity is within a factor of two of the photon flux inferred from the X-ray flux at the time of our observations, assuming that the spectral shape has indeed remained constant. This drop in the He II luminosity indicates that the *total* X-ray luminosity must have decreased, rather than merely that in our line of sight. This argues against partial obscuration by a precessing accretion disk, which would not affect the total X-ray luminosity seen by the He II-emitting region. Instead, it suggests either an overall increase of obscuring material, possibly due to increased outflow from the accretion disk, or an intrinsic drop in the X-ray luminosity. However, it is unclear how either of these scenarios can be made compatible with the lack of variability in the X-ray spectral shape and, for the latter scenario in particular, with the constant spin-up rate of the pulsar.

4.6. Conclusions

NGC 300 ULX-1 is the second known ULX pulsar with a supergiant donor star (the other being NGC 7793 P13, which has a B9I companion, Motch et al. 2011, 2014). The other four ULX pulsars known to date all have orbital periods of only a few days (Bachetti et al. 2014; Israel et al. 2017; Rodríguez Castillo et al. 2019; Sathyaprakash et al. 2019), implying that they likely have main sequence or Hertzsprung gap donors, although those are too faint to be detected in these extragalactic systems (Heida et al. 2019). Among the general population of ULXs, three other sources have counterparts that have been spectroscopically identified as RSGs (Heida et al. 2015, 2016), and Lau et al. (2019) identified two others as likely RSGs based on their MIR colors.

This small but significant fraction (two out of six ULX pulsars, and at least four to six out of $\sim$150 ULXs within 10 Mpc) with supergiant donors is an extremely interesting subset of ULXs, especially because they may be progenitors of

binary compact object mergers (e.g., Belczynski et al. 2016). ULXs with supergiant donors are currently underproduced by binary population synthesis codes (e.g., Wiktorowicz et al. 2017, who find RSG donors in <1% of systems). This may be due to the fact that these codes do not take mass transfer through (focused) wind mass loss into account, and shows that this phenomenon may play an important role in ULXs with RSG donor stars.

SN2010da/NGC 300 ULX-1 is the only ULX to date that is also associated with an ILOT; vice versa, it is also the only ILOT that has turned into an X-ray binary post-explosion, as well as the only one that contains a spectroscopically confirmed RSG star. This unique system has the potential to offer insights into the formation of supergiant ULXs and episodic mass loss from evolved massive stars; for example, it is possible that the 2010 outburst was related to a common envelope phase, or to a tidal interaction in a very eccentric binary system. Long-term monitoring of both the X-ray source and the optical/NIR spectrum is necessary to determine the orbital period and discriminate between different scenarios. Late-time follow-up of similar ILOTs with X-ray telescopes may reveal other supergiant ULXs and shed light on the evolutionary pathways that produce these systems.

M.H. would like to thank M. Bachetti, E. Levesque, G. Vasilopoulos, I. el Mellah, S. Guillot, and E. Quatart for useful discussions. Based on observations collected at the European Organisation for Astronomical Research in the Southern Hemisphere under ESO programme(s) 102.D-0535(A).

Facility: VLT(X-shooter).

Software: Astropy (Astropy Collaboration et al. 2013), Reflex (Freudling et al. 2013), Molecfit (Kausch et al. 2015; Smette et al. 2015), TURBOSPECTRUM (Plez 2012).

ORCID iDs

M. Heida https://orcid.org/0000-0002-1082-7496
B. Davies https://orcid.org/0000-0002-2010-2122
F. Fürst https://orcid.org/0000-0003-0388-0560
B. W. Grefenstette https://orcid.org/0000-0002-1984-2932
J. A. Kennea https://orcid.org/0000-0002-6745-4790
F. Tramper https://orcid.org/0000-0001-8631-7700
D. J. Walton https://orcid.org/0000-0001-5819-3552

References

Ambrosi, E., & Zampieri, L. 2018, MNRAS, 480, 4918
Astropy Collaboration, Robitaille, T. P., Tollerud, E. J., et al. 2013, A&A, 558, A33
Bachetti, M., Harrison, F. A., Walton, D. J., et al. 2014, Natur, 514, 202
Belczynski, K., Holz, D. E., Bulik, T., & O'Shaughnessy, R. 2016, Natur, 534, 512
Binder, B., Levesque, E. M., & Dorn-Wallenstein, T. 2018, ApJ, 863, 141
Binder, B., Williams, B. F., Kong, A. K. H., et al. 2011, ApJL, 739, L51
Binder, B., Williams, B. F., Kong, A. K. H., et al. 2016, MNRAS, 457, 1636
Carpano, S., Haberl, F., Maitra, C., & Vasilopoulos, G. 2018, MNRAS: Letters, 476, L45
Choi, J., Dotter, A., Conroy, C., et al. 2016, ApJ, 823, 102
Chornock, R., & Berger, E. 2010, ATel, 2637, 1
Copperwheat, C., Cropper, M., Soria, R., & Wu, K. 2005, MNRAS, 362, 79
Dalcanton, J. J., Williams, B. F., Seth, A. C., et al. 2009, ApJS, 183, 67
Davies, B., Crowther, P. A., & Beasor, E. R. 2018, MNRAS, 478, 3138
Davies, B., Kudritzki, R.-P., Gazak, Z., et al. 2015, ApJ, 806, 21
Davies, B., Kudritzki, R.-P., Plez, B., et al. 2013, ApJ, 767, 3
Davies, B., Origlia, L., Kudritzki, R.-P., et al. 2009, ApJ, 696, 2014
Eggleton, P. P. 1983, ApJ, 268, 368
El Mellah, I., Sundqvist, J. O., & Keppens, R. 2019, A&A, 622, L3
Elias–Rosa, N., Mauerhan, J. C., & van Dyk, S. D. 2010, ATel, 2636, 1
Fabrika, S., Ueda, Y., Vinokurov, A., Sholukhova, O., & Shidatsu, M. 2015, NatPh, 11, 551
Freudling, W., Romaniello, M., Bramich, D. M., et al. 2013, A&A, 559, A96
Fürst, F., Walton, D. J., Heida, M., et al. 2018, A&A, 616, A186
Gazak, J. Z., Kudritzki, R., Evans, C., et al. 2015, ApJ, 805, 182
Gustafsson, B., Edvardsson, B., Eriksson, K., et al. 2008, A&A, 486, 951
Heida, M., Harrison, F. A., Brightman, M., et al. 2019, ApJ, 871, 231
Heida, M., Jonker, P. G., Torres, M. A. P., et al. 2016, MNRAS, 459, 771
Heida, M., Torres, M. A. P., Jonker, P. G., et al. 2015, MNRAS, 453, 3510
Israel, G. L., Belfiore, A., Stella, L., et al. 2017, Sci, 355, 817
Kaaret, P., Feng, H., & Roberts, T. P. 2017, ARA&A, 55, 303
Kausch, W., Noll, S., Smette, A., et al. 2015, A&A, 576, A78
Kosec, P., Pinto, C., Walton, D. J., et al. 2018, MNRAS, 479, 3978
Lau, R. M., Heida, M., Walton, D. J., et al. 2019, ApJ, 878, 71
Lau, R. M., Kasliwal, M. M., Bond, H. E., et al. 2016, ApJ, 830, 142
Meyer, M. R., Edwards, S., Hinkle, K. H., & Strom, S. E. 1998, ApJ, 508, 397
Monard, L. A. G. 2010, CBET, 2289, 1
Moon, D.-S., Harrison, F. A., Cenko, S. B., & Shariff, J. A. 2011, ApJL, 731, L32
Motch, C., Pakull, M. W., Grisé, F., & Soria, R. 2011, AN, 332, 367
Motch, C., Pakull, M. W., Soria, R., Grisé, F., & Pietrzyński, G. 2014, Natur, 514, 198
Ohnaka, K., Weigelt, G., & Hofmann, K.-H. 2017, Natur, 548, 310
Pakull, M. W., & Angebault, L. P. 1986, Natur, 322, 511
Pakull, M. W., & Mirioni, L. 2002, arXiv:0202488
Pakull, M. W., Soria, R., & Motch, C. 2010, Natur, 466, 209
Plez, B. 2012, Turbospectrum: Code for spectral synthesis, Astrophysics Source Code Library, ascl:1205.004
Prieto, J. L., Bond, H. E., Kochanek, C. S., et al. 2010, ATel, 2660, 1
Quast, M., langer, N., & Tauris, T. M. 2019, A&A, 628, A19
Ray, P. S., Guillot, S., Ho, W. C. G., et al. 2019, ApJ, 879, 130
Richards, A. M. S., & Yates, J. A. 1998, IrAJ, 25, 7
Roberts, T. P., Gladstone, J. C., Goulding, A. D., et al. 2011, AN, 332, 398
Rodríguez Castillo, G. A., Israel, G. L., Belfiore, A., et al. 2019, arXiv:1906.04791
Sathyaprakash, R., Roberts, T. P., Walton, D. J., et al. 2019, MNRAS: Letters, 488, L35
Schlafly, E. F., & Finkbeiner, D. P. 2011, ApJ, 737, 103
Smette, A., Sana, H., Noll, S., et al. 2015, A&A, 576, A77
Smith, N., Ganeshalingam, M., Chornock, R., et al. 2009, ApJL, 697, L49
van den Heuvel, E. P. J., Portegies Zwart, S. F., & de Mink, S. E. 2017, MNRAS, 471, 4256
Van Dyk, S. D., Peng, C. Y., King, J. Y., et al. 2000, PASP, 112, 1532
van Loon, J. T., Zijlstra, A. A., Bujarrabal, V., & Nyman, L. Å. 2001, A&A, 368, 950
Vasilopoulos, G., Haberl, F., Carpano, S., & Maitra, C. 2018, A&A, 620, L12
Vasilopoulos, G., Petropoulou, M., Koliopanos, F., et al. 2019, MNRAS, 488, 5225
Vernet, J., Dekker, H., D'Odorico, S., et al. 2011, A&A, 536, A105
Villar, V. A., Berger, E., Chornock, R., et al. 2016, ApJ, 830, 11
Walton, D. J., Bachetti, M., Fürst, F., et al. 2018b, ApJL, 857, L3
Walton, D. J., Fürst, F., Heida, M., et al. 2018a, ApJ, 856, 128
Westmeier, T., Braun, R., & Koribalski, B. S. 2011, MNRAS, 410, 2217
Wiktorowicz, G., Sobolewska, M., Lasota, J.-P., & Belczynski, K. 2017, ApJ, 846, 17